# Self-similarity in single-point turbulent statistics across different quadrants in turbulent rotor wakes

Xue-Lu Xiong (熊雪露),[1] Shujin Laima (赖马树金),[2,3]
Hui Li (李惠),[2,3,4] and Yi Zhou (周毅)[1,*]

[1]*School of Energy and Power Engineering, Nanjing University of Science and Technology, Nanjing 210094, China*

[2]*Key Lab of Smart Prevention and Mitigation of Civil Engineering Disasters of the Ministry of Industry and Information Technology, Harbin Institute of Technology, Harbin 150090, China*

[3]*Key Lab of Structures Dynamic Behavior and Control of the Ministry of Education, Harbin Institute of Technology, Harbin 150090, China*

[4]*Guangdong-Hong Kong-Macao Joint Laboratory for Data-Driven Fluid Mechanics and Engineering Applications, Harbin Institute of Technology (Shenzhen), Shenzhen 518055, China*

(Received 5 December 2023; accepted 30 April 2024; published 22 May 2024)

This paper presents a quadrant analysis of turbulent rotor wakes, placing a particular emphasis on the self-similarity in single-point turbulent statistics. The self-similarity analysis reveals that within the wake self-similar region, the distribution of the Reynolds shear stress $-\overline{u'v'}$ and the turbulent kinetic energy $k$ in different quadrants can also attain a state of self-similarity. The length scaling is the same for $-\overline{u'v'}$, $k$, and their different quadrant contributions. However, the velocity scaling of the ejection contribution differs from that of $-\overline{u'v'}$ and $k$. Additionally, the analysis of hole filtering and spectrum filtering effects on the self-similarity and scaling of the ejection contribution to $-\overline{u'v'}$ reveals a strong connection between ejection events and large-scale coherent structures, as well as deceleration extreme events. This finding is further confirmed through quadrant analysis of the time evolution of velocity fluctuations. The present study can be helpful in improving our understanding of the turbulent wake self-similarity.

DOI: 10.1103/PhysRevFluids.9.054608

## I. INTRODUCTION

Numerous studies have demonstrated that turbulent wakes can attain a state of self-similarity/self-preservation in the far wake region [1–9]. The self-similar state of turbulent wakes refers to the lateral distribution of single-point turbulent statistics evolving with streamwise distance while maintaining a geometric similarity [10]. For instance, in the case of the Reynolds shear stress $-\overline{u'v'}$ in axisymmetric turbulent wakes, self-similarity implies that $-\overline{u'v'}(x, r) = R_s(x)g[r/\delta(x)]$, with the normalized distribution function, $g$, remaining consistent at different streamwise locations. Note that the streamwise evolution of the characteristic scales, $R_s(x)$ and $\delta(x)$, is often referred to as the scaling laws [4,5,9]. The self-similarity of turbulent wakes holds both research and engineering application significance, i.e., prerequisites for the development of an analytical prediction model of wind turbine wake [11–19].

However, the development of turbulent wake self-similarity theory has been hindered by the complexities introduced by turbulent energy transport and turbulent dissipation, which are closely intertwined with the self-similarity and scaling laws of turbulent wakes [1–5,9]. Moreover, the root

*yizhou@njust.edu.cn

 ©2024 American Physical Society

cause of the turbulent wake self-similarity, or in other words, why some wake profiles can reach a self-similar state is not clear as stated by Vassilicos [20]. It is well known that the Reynolds shear stress plays a pivotal role in turbulent energy transport. Therefore, an in-depth study of the Reynolds shear stress and the evolution of its self-similar state can improve our understanding of the physics underlying turbulent wake self-similarity.

As early as the 1970s, it was found that the Reynolds stress is closely related to the vortex stretching, as documented in the textbook by Tennekes and Lumley [1]. Subsequently, the work of Philip and Marusic [21] demonstrated that a random collection of coherent large-scale eddies is sufficient for describing the first- and second-order turbulence statistics in axisymmetric jets and wakes. More recently, Chen *et al.* [22] revealed that when large-scale vortices prevail, the Reynolds shear stress associated with the coherent motion is a good approximation to the conventional Reynolds shear stress. Thus, the root cause of the self-similarity of the Reynolds shear stress profiles or the self-similarity of turbulent wake profiles can be explored via the self-similarity analysis of large-scale vortices or large-scale coherent structures. Note that the concept of studying flow through coherent structures is not novel, since about 60 years ago Kühemann [23] described the vortex motion as "the sinews and muscles of fluid motions."

To characterize the vortex motions or coherent structures within a flow field, three-dimensional flow field data are typically needed, which is a straightforward task in numerical simulations. However, in the context of experimental measurements, which are more feasible for high Reynolds number flows, acquiring three-dimensional flow field data presents significant challenges. In most of the scenarios, the available data are limited to single-point velocity measurements, obtained using instruments such as hot wires, Cobra probes, or anemometers. While deriving coherent structures from single-point measurements is a nontrivial endeavor, various analytical methods can partially address this challenge, e.g., spectrum analysis, quadrant analysis, etc.

Quadrant analysis initially conceived and applied fifty years ago by Wallace *et al.* [24] has gained widespread adoption in the context of the Reynolds shear stress analysis to study the coherent structures of shear flows [15,25–28]. Studies have demonstrated that the distribution of Reynolds shear stress in the ejection quadrant (quadrant two) and sweep quadrant (quadrant four) closely correlates with the vortex structures [29,30]. Recently Yin *et al.* [27] identified a similarity in the profiles of the Reynolds shear stress across different quadrants at various streamwise locations in the far wake region of an axisymmetric turbulent wake. However, the scaling laws of different quadrant contributions and the effect of coherent structures across different scales on the self-similarity characteristics exhibited by the contribution from different quadrants to single-point turbulent statistics are still unclear.

The Reynolds shear stress plays a pivotal role in understanding turbulent energy transport and the self-similar state within turbulent wakes. There is a close connection between ejection and sweep events and the coherent structures. Therefore, the main purpose of this study is to investigate the self-similarity state of these different quadrant contributions. We also consider the impact of hole filtering and spectrum filtering to unveil the intricate relationship between contributions from different quadrants, large-scale coherent structures, and extreme events. Note that the extreme events, characterized by velocity fluctuations with probability distribution deviating from Gaussian distributions and exhibiting larger flatness compared to their Gaussian counterparts [31–36], are closely correlated with intense velocity fluctuations and the Reynolds shear stress.

The remainder of this paper is organized as follows. The experimental data and theoretical background of quadrant analysis are described in Sec. II. The distribution of the Reynolds shear stress $-\overline{u'v'}$ and the turbulent kinetic energy in each quadrant is then presented in Sec. III. The self-similarity state of different quadrant contributions are discussed in Sec. IV A. The effect of hole filtering and spectrum filtering on the self-similarity and scaling laws are presented in Secs. IV B and IV C, respectively. The time distribution of each quadrant contribution is studied in Sec. V. Finally, main conclusions are drawn in Sec. VI.

TABLE I. Key parameters and operation condition of the rotor.

| $U_\infty$(m/s) | $D$(mm) | $\Omega$(r/min) | $\lambda$ | $\mathrm{Re}_D$ |
|---|---|---|---|---|
| 10.4 | 65 | 9700 | 3.17 | $4.6 \times 10^4$ |

## II. EXPERIMENT SETUP AND THEORY BACKGROUND

### A. Experiment setup

The data used in this study are derived from the rotor wake experiments conducted by Xiong *et al.* [9]. Note that numerous studies have confirmed the similarity between the rotor wakes and other canonical axisymmetric wakes in the far wake region [37–42]. Therefore, the findings in the present study can be extended to other canonical axisymmetric wakes. With detailed information on the experiment setup available in Ref. [9], in this section, only the key parameters of the experiments are presented for reference. The experiments were performed in an open circuit wind tunnel with the test section measuring 450 mm (width) × 430 mm (height) × 2500 mm (length). Uniform and steady inflow with free-stream velocity $U_\infty = 10.4$ m/s and turbulence intensity below 0.6% was maintained in all experiments. A two-blade rotor model (GWS/EP − 2510 × 2) with diameter $D = 65$ mm was used to simulate the wind turbine rotor wake. The Reynolds number based on the inflow velocity $U_\infty$ and rotor diameter $D$ is $\mathrm{Re}_D = U_\infty D/\nu \approx 4.6 \times 10^4$, where $\nu$ is the kinematic viscosity. According to the study of Chamorro *et al.* [43] and Xiong *et al.* [17], the mean velocity and high-order turbulence statistics of the rotor far wake are independent of the Reynolds number when $\mathrm{Re}_D$ is larger than $4.6 \times 10^4$. Therefore, the results of this study can provide useful information for engineering applications, i.e., in enhancing the understanding of the full-scale wind turbine wakes. Throughout the experiments, the rotor rotation speed $\Omega$ was selected to be $\Omega = 9700$ r/min, with the corresponding tip-speed ratio being $\lambda = 0.5 \times \Omega D/U_\infty \approx 3.17$. The key parameters and operation conditions of the rotor model are listed in Table I.

Figure 1 illustrates the wake measurements setup in the experiments. A Cartesian coordinate system $(x, y, z)$ with its origin set at the rotor center is used, where $x$, $y$, and $z$ represent the streamwise, horizontal, and vertical directions, respectively. A Cobra probe Anemometry system (TFI Series 100, Turbulent Flow Instrumentation), which can measure velocity fluctuations characterized by frequencies lower than 1250 Hz, was used to obtain the three velocity components $u$, $v$, $w$ in the $x$, $y$, $z$ directions, respectively. The data were sampled at 5 kHz for a duration of 60 s during the experiments. The lateral measurement region was $-2.12 \leqslant y/D \leqslant 2.12$ and the

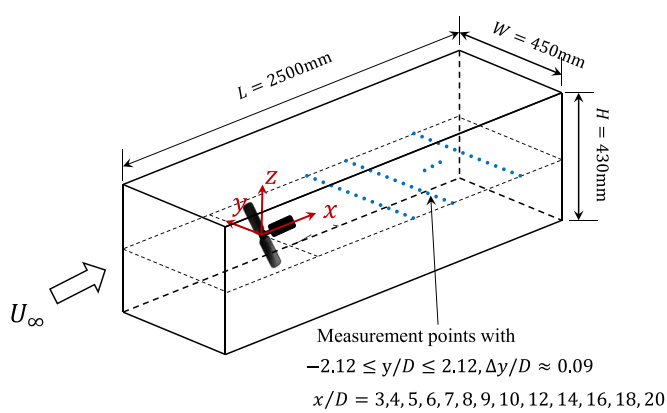


FIG. 1. Illustration of the experimental setup.

TABLE II. Key parameters of the measuring/experimental instruments.

| Position error | Frequency response | Flow velocity | Flow angle | Angle accuracy |
|---|---|---|---|---|
| $\leqslant$0.1 mm | 0 to $\geqslant$2000 Hz | 2–100 m/s | $\pm 45^{\circ}$ cone | $\pm 1.0^{\circ}$ |

streamwise measurement locations were $x/D = 3, 4, 5, 6, 7, 8, 9, 10, 12, 14, 16, 18, 20$, as shown in Fig. 1. Some key parameters of the measuring/experimental instruments are listed in Table II.

### B. Quadrant analysis

Quadrant analysis, originally conceived and applied by Wallace *et al.* [24], has been widely applied to the Reynolds shear stress analysis to study the its relationship with coherent structures in turbulent wakes [15,25–28]. Based on the direction of velocity fluctuations $u'$ and $v'$, quadrant analysis [29] divides the Reynolds shear stress $-\overline{u'v'}$ into four quadrants ($Q1$–$Q4$), as illustrated in Fig. 2. The average contribution of quadrant $i$ to $-\overline{u'v'}$ is defined as $-\overline{u'v'}_{Qi}$, which is computed as

$$-\overline{u'v'}_{Qi} = \frac{1}{N}\sum_{n=1}^{N}[-u'v'I_i(u', v')]_n, \tag{1}$$

$$I_i(u',v') = \begin{cases} 1, & \text{if } (u', v') \text{ in quadrant } i \\ 0, & \text{otherwise} \end{cases}. \tag{2}$$

According to the above definition, we have $\overline{u'v'} = \overline{u'v'}_{Q1} + \overline{u'v'}_{Q2} + \overline{u'v'}_{Q3} + \overline{u'v'}_{Q4}$. The ejection contribution to $-\overline{u'v'}$ ($-\overline{u'v'}_{Q2}$) and sweep contribution to $-\overline{u'v'}$ ($-\overline{u'v'}_{Q4}$) are crucial for energy transport [29], which also can be seen from Fig. 2. For further information, one may refer to Ref. [29] and the references cited therein.

## III. QUADRANT CONTRIBUTION

First, the distribution of the Reynolds shear stress $-\overline{u'v'}$ and the turbulent kinetic energy $k$ in different quadrants is analyzed. The lateral profiles of the quadrant distribution of the Reynolds shear stress ($-\overline{u'v'}_{Qi}$) are plotted in Fig. 3 for different streamwise locations. It is obvious that the distribution of the Reynolds shear stress $-\overline{u'v'}$ in $Q2$ (ejection) is predominate, particularly in the outer part of the wake ($\approx 0.3L_b \sim 1.0L_b$, where $L_b$ denotes the half-width of the wake distribution), while in the near wake region, $Q4$ (sweep) also makes a significant contribution in the inner part of the wake ($\approx 0.0L_b \sim 0.3L_b$). The peak positions of $-\overline{u'v'}_{Q2}$ profiles are situated farther outward than those of $-\overline{u'v'}$, while the peak positions of $-\overline{u'v'}_{Q4}$ profiles are located more inward than those

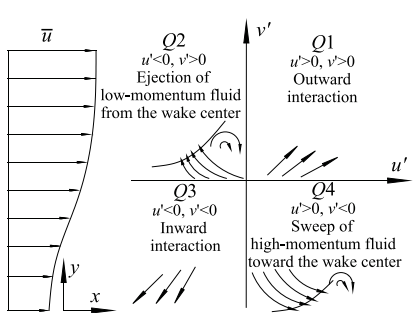


FIG. 2. Sketch of quadrant distribution for a turbulent wake.

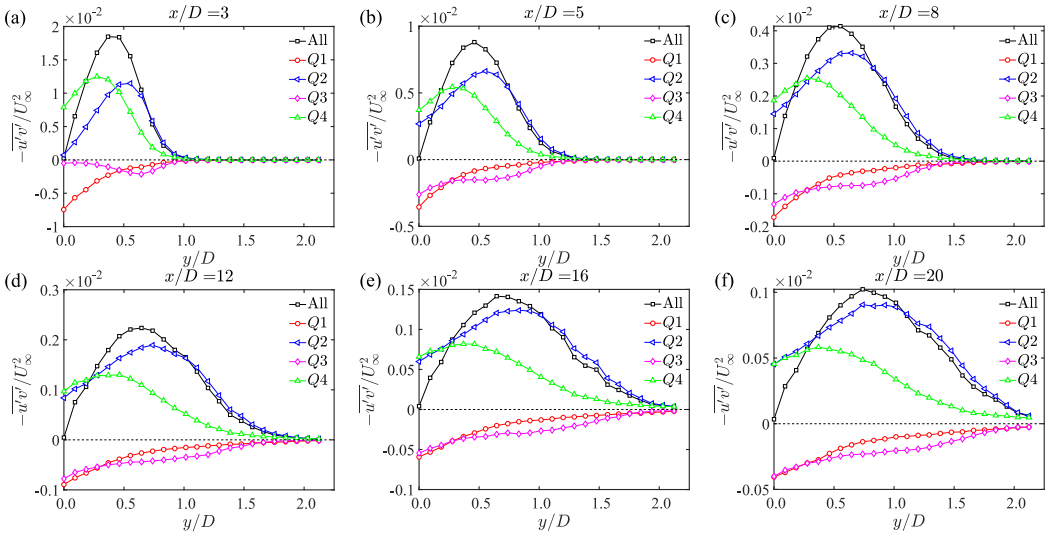


FIG. 3. Lateral profiles of the Reynolds shear stress $-\overline{u'v'}$ and its distribution in four different quadrants at some streamwise locations: (a) $x/D = 3$, (b) $x/D = 5$, (c) $x/D = 8$, (d) $x/D = 12$, (e) $x/D = 16$, and (f) $x/D = 20$.

of $-\overline{u'v'}$. This observation suggests that high-momentum fluids are transported toward the wake central region, while low-momentum fluids are transported toward the ambient flow.

Moreover, in the outer part of the wake, $-\overline{u'v'}_{Q2} \approx -\overline{u'v'}$, indicates that $-\overline{u'v'}$ can be effectively represented by its contribution in $Q2$ in this region. In the central wake region, the absolute value of $-\overline{u'v'}_{Qi}$ is approximately the same for all four quadrants, particularly in the far wake region. This observation implies that $-\overline{u'v'} \approx 0$ in the central wake region according to Eq. (1), indicating a higher degree of isotropic in the turbulence within the central region compared to the outer region of the wake. This observation aligns with previous findings indicating that large-scale motions are predominantly founded at the outer edges of the wake, while the central wake region is primarily characterized by small-scale motions [28,44].

Similar to the definition of the quadrant distribution of the Reynolds shear stress ($-\overline{u'v'}_{Qi}$), we can define a quadrant distribution of the turbulent kinetic energy $k$ as

$$k_{Qi} = \frac{1}{N}\sum_{n=1}^{N}\left[\frac{1}{2}(u'u' + v'v' + w'w')I_i(u', v')\right]_n. \tag{3}$$

Figure 4 shows the lateral profiles of $k_{Qi}$ at different streamwise locations. From Fig. 4 one can conclude that the quadrant distribution of $k$ is similar to the quadrant distribution of $-\overline{u'v'}$. Moreover, in the far wake region, despite the peak positions of the lateral profiles of $k$ being located at the wake center, the peak positions of the lateral profiles of $k_{Q2}$ and $k_{Q4}$ are approximately the same as the peak positions of the lateral profiles of $-\overline{u'v'}_{Q2}$ and $-\overline{u'v'}_{Q4}$, respectively. Note that, different from $-\overline{u'v'}_{Q2} \approx -\overline{u'v'}$ in the outer part of the wake, $k_{Q2} < k$ in the outer part of the wake, since the distribution of $k$ in all four quadrants is positive.

In conclusion, $-\overline{u'v'}_{Q2}$ plays a dominant contribution to $-\overline{u'v'}$, and $-\overline{u'v'}_{Q2} \approx -\overline{u'v'}$ in the outer part of the wake suggests that the momentum transported from ambient flow to the wake region is primarily due to the ejection events. Moreover, the quadrant distribution of $k$ is similar to the quadrant distribution of $-\overline{u'v'}$, with the peak positions of the lateral profiles of $k_{Q2}$ and $k_{Q4}$ aligning closely with the peak positions of the lateral profiles of $-\overline{u'v'}_{Q2}$ and $-\overline{u'v'}_{Q4}$, respectively.

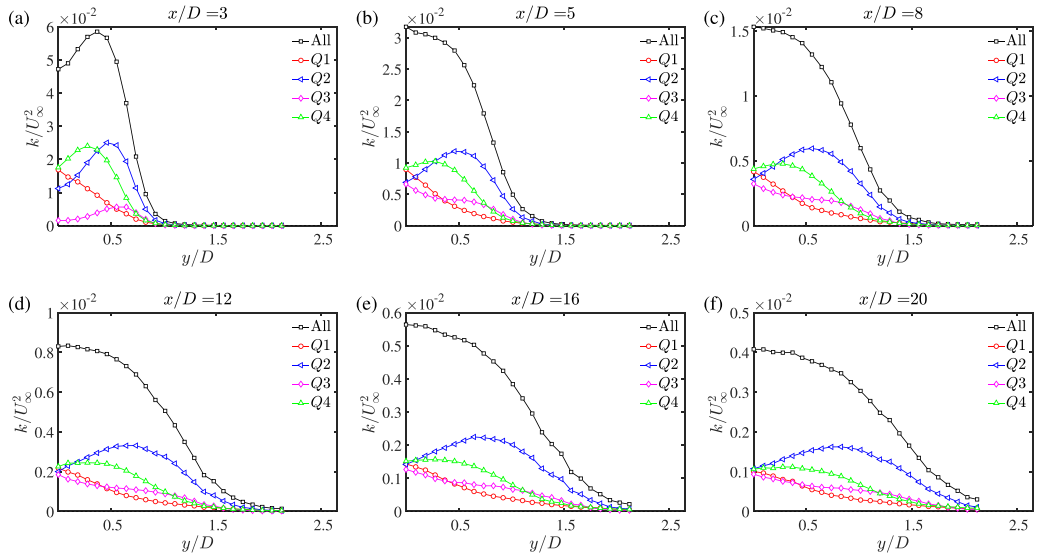


FIG. 4. The same as Fig. 3 but for the turbulent kinetic energy $k$.

## IV. SELF-SIMILARITY OF QUADRANT CONTRIBUTION

In this section, the self-similarity of different quadrant contributions of $-\overline{u'v'}$ and $k$ will be analyzed in detail. As demonstrated in Sec. III, ejection events ($Q2$) make the most contributions to $-\overline{u'v'}$ and $k$. Given the well-established connection between ejection events and coherent structures in previous research [29], this section will focus on the self-similar state of ejection events contribution and its relationship with coherent structures.

### A. Self-similarity state of different quadrant contributions

To perform the self-similarity analysis, two different characteristic scales are first defined. For the lateral profiles of $-\overline{u'v'}$, as illustrated in Fig. 5, the characteristic length scale $\delta$ is defined as the distance between the wake center and the peak position of the lateral profile, and the characteristic velocity scale $\sqrt{R_s}$ is defined as the square root of the peak value of the lateral profile. Note that the definition of the characteristic velocity scale $\sqrt{R_{s,Qi}}$, $\sqrt{K_s}$, and $\sqrt{K_{s,Qi}}$ for the lateral profiles of $-\overline{u'v'}_{Qi}$, $k$, and $k_{Qi}$, respectively, is similar to the definition of the characteristic velocity scale $\sqrt{R_s}$ for the lateral profiles of $-\overline{u'v'}$.

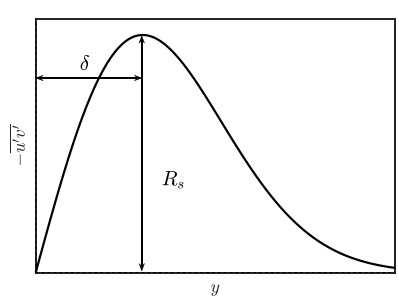


FIG. 5. Definition of the characteristic parameters for the Reynolds shear stress $-\overline{u'v'}$.

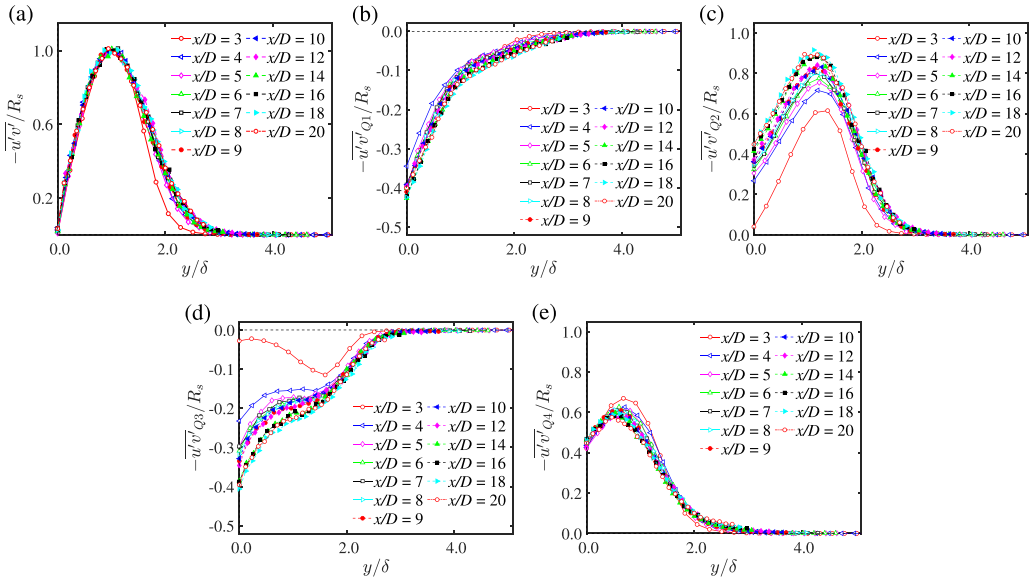


FIG. 6. Self-similarity in the normalized profiles of (a) $-\overline{u'v'}$, (b) $-\overline{u'v'}_{Q1}$, (c) $-\overline{u'v'}_{Q2}$, (d) $-\overline{u'v'}_{Q3}$, and (e) $-\overline{u'v'}_{Q4}$.

The normalized profiles of $-\overline{u'v'}$ and its corresponding quadrant contribution $-\overline{u'v'}_{Qi}$ are shown in Fig. 6. Consistent with our previous research [9], when normalized by $\delta$ and $R_s$, the lateral profiles of $-\overline{u'v'}$ exhibit excellent collapse into a single line in the region $x/D \geqslant 4$. Concerning the quadrant contributions, the normalized lateral profiles of $-\overline{u'v'}_{Q1}$ and $-\overline{u'v'}_{Q4}$ can also be well collapsed into a single line in the region $x/D \geqslant 4$, while the normalized lateral profiles of $-\overline{u'v'}_{Q2}$ and $-\overline{u'v'}_{Q3}$ only can be well collapsed into a single line in the region $x/D \geqslant 14$. Note that, even though the normalized profiles of $-\overline{u'v'}_{Q2}$ do not collapse into a single line in the region $4 \leqslant x/D \leqslant 14$, their normalized peak positions remain consistent. This implies that despite the difference in velocity scaling between $-\overline{u'v'}_{Q2}$ and $-\overline{u'v'}$, their length scaling remains the same.

Similarly, we can define the corresponding characteristic velocity scale $\sqrt{R_{s,Qi}}$ for the lateral profiles of $-\overline{u'v'}_{Qi}$, and use $R_{s,Qi}$ and $\delta$ for the normalization. Figures 7(a) and 7(c) show that the profiles of $-\overline{u'v'}_{Q2}$ and $-\overline{u'v'}_{Q3}$ can be well collapsed into a single line in the region $x/D \geqslant 4$ when normalized by $R_{s,Qi}$ and $\delta$. Moreover, Fig. 7(b) shows that there is an increase in the ratio $R_{s,Q2}/R_s$ in the streamwise direction within the measurement region, although this trend is less pronounced in the region $14 \leqslant x/D \leqslant 20$. This suggests a growing contribution of ejection events to the total Reynolds shear stress $-\overline{u'v'}$ in this region. To maintain balance, there is also an increase in the absolute value of the ratio $R_{s,Q3}/R_s$ in this region ($R_{s,Q2}/R_s > 0$, $R_{s,Q3}/R_s < 0$), as shown in Fig. 7(d), signifying that the increased contribution of ejection events ($Q2$) is accompanied by an increased contribution of inward interaction ($Q3$).

In our previous research [9], we revealed that $R_s/U_s^2$ increase with $x$ in the region $5 \leqslant x/D \leqslant 12$, and transitions to $R_s/U_s^2 \sim$ constant in the region $x/D \geqslant 12$, where $U_s$ is the characteristic velocity scale of the velocity deficit profile. Note that the constant eddy viscosity hypothesis assumes the eddy viscosity to be $\nu_T = \alpha U_s \delta$ [45–47]. Through the momentum conservation equation, we have that $R_s = \alpha U_s^2$. Thus, $\alpha \neq$ constant in the region $5 \leqslant x/D \leqslant 12$, and $\alpha =$ constant in the region $x/D \geqslant 12$. Apparently, the self-similarity state is different for these two region. There we define the self-similarity region with $\alpha \neq$ constant as "stage I" and define the self-similarity region with $\alpha =$ constant as "stage II." The start position of self-similarity stage I ($\alpha \neq$ constant) and

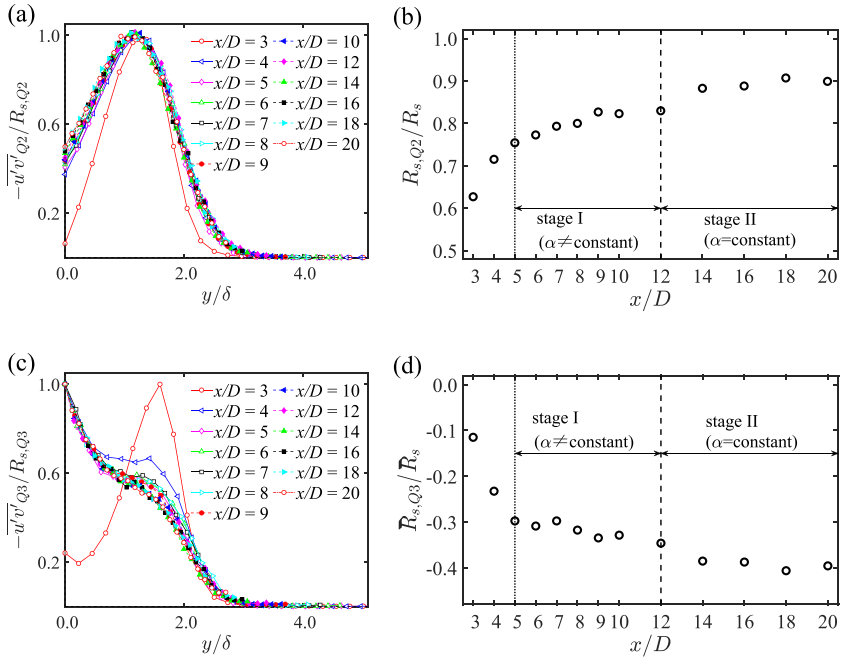


FIG. 7. Self-similarity and scaling law of $-\overline{u'v'}_{Q2}$ and $-\overline{u'v'}_{Q3}$. (a), (c) The normalized profiles of $-\overline{u'v'}_{Q2}$ and $-\overline{u'v'}_{Q3}$; (b), (d) the streamwise evolution of the ratio $R_{s,Q2}/R_s$ and $R_{s,Q3}/R_s$. The vertical dotted and dashed lines in (b) and (d), denoting the start position of self-similarity stage I ($\alpha \neq$ constant) and self-similarity stage II ($\alpha =$ constant), respectively, are plotted based on Ref. [9].

self-similarity stage II ($\alpha =$ constant) is indicated by vertical dotted and dashed lines, respectively, in Figs. 7(b) and 7(d) for ease of reference.

By considering momentum conservation in the self-similar region of an axisymmetric wake, we can theoretically derive the relationship $U_s\delta^2 \sim$ constant. Thus, $R_s\delta^4 \sim \alpha$ with $\alpha \neq$ constant in the region $5 \leqslant x/D \leqslant 12$, and $\alpha =$ constant in the region $x/D \geqslant 12$. The above analysis demonstrates that the length scaling of the profiles of $-\overline{u'v'}$ and $-\overline{u'v'}_{Qi}$ is the same. Thus, we can define the self-similarity stage of different quadrant contribution in terms of $R_{s,Qi}/R_s$. Figures 7(b) and 7(d) illustrate an increasing absolute value of $R_{s,Q2}/R_s$ and $R_{s,Q3}/R_s$ in the streamwise direction, which indicates that $R_{s,Q2}\delta^4 \neq$ constant and $R_{s,Q3}\delta^4 \neq$ constant. This suggests that the contribution of $Q2$ and $Q3$ is in a state of self-similarity stage I in the whole measurement region, regardless of the self-similarity stage of $-\overline{u'v'}$. Figures 7(b) and 7(d) show that $R_{s,Q2}/R_s$ and $R_{s,Q3}/R_s$ eventually approach a constant, indicating that the contribution of $Q2$ and $Q3$ will reach a state of self-similarity stage II farther downstream. As for $Q1$ and $Q4$, since the velocity scaling of $-\overline{u'v'}_{Q1}$, $-\overline{u'v'}_{Q4}$ and $-\overline{u'v'}$ is the same, their self-similarity state is the same.

Similar to the definition of the characteristic velocity scale $\sqrt{R_s}$ and $\sqrt{R_{s,Qi}}$ for the Reynolds shear stress $-\overline{u'v'}$ and its quadrant distribution $-\overline{u'v'}_{Qi}$, the corresponding characteristic value $\sqrt{K_s}$ and $\sqrt{K_{s,Qi}}$ for the turbulent kinetic energy $k$ and its quadrant distribution $k_{Qi}$ can be defined and used for the normalization. Figures 8 and 9 show that the streamwise evolution of the self-similarity state of $k_{Qi}$ is similar to $-\overline{u'v'}_{Qi}$. Moreover, previous research confirmed the assumption of constant anisotropy is valid when the wake reaches a state of self-similarity [5,9]. According to the assumption of constant anisotropy, $-\overline{u'v'}$ and $k$ evolves synchronously in the streamwise direction ($R_s/K_s =$ constant). The above analysis shows that their distribution in $Q1$ and $Q4$ also evolves synchronously in the streamwise direction when the wake reaches a state of self-similarity. Figure 10 shows the streamwise evolution of $R_{s,Q2}/K_{s,Q2}$. It is clear that $R_{s,Q2}/K_{s,Q2}$ approximates

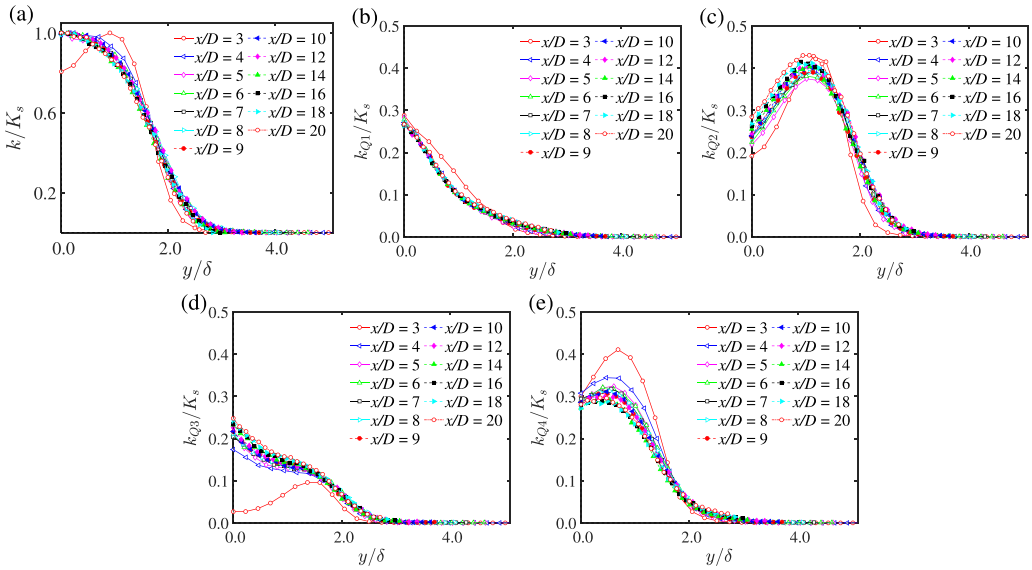


FIG. 8. Self-similarity in the normalized profiles of (a) $k$, (b) $k_{Q1}$, (c) $k_{Q2}$, (d) $k_{Q3}$, and (e) $k_{Q4}$.

a constant in the region $x/D \geqslant 4$, suggesting that the distribution of $-\overline{u'v'}$ and $k$ in $Q2$ also evolves synchronously in the streamwise direction in the self-similar region. Thus, the constant anisotropy assumption remains valid for different quadrant contributions in the self-similar region.

In conclusion, the distribution of $-\overline{u'v'}$ and $k$ in different quadrants can also reach a self-similar state in the wake self-similar region, with consistent length scaling for $-\overline{u'v'}$, $k$ and their distribution in different quadrants. However, their velocity scaling is different in the case of their distribution in $Q2$ and $Q3$. The self-similarity state of $-\overline{u'v'}$ is the combined effects of all four quadrant contributions. The two components $-\overline{u'v'}_{Q2}$ and $-\overline{u'v'}_{Q3}$ are expected to reach self-similarity stage II farther downstream compared to $-\overline{u'v'}$. Moreover, the constant anisotropy assumption remains valid for different quadrant contributions in the self-similar region.

### B. Hole filtering effect on the self-similar state of different quadrant contributions

The above analysis shows that momentum transported from ambient flow to the wake region is primarily due to ejection events ($Q2$), and the velocity scaling of $-\overline{u'v'}_{Q2}$ is different from that of $-\overline{u'v'}$. Note that the above analysis considers full fluctuation components. In this section quadrant hole filtering is applied to explore the contribution of the intense Reynolds shear stress to the self-similar state of $-\overline{u'v'}_{Q2}$. The quadrant hole filtering method (Fig. 11) is defined as

$$-\overline{u'v'}_{Qi,H} = \frac{1}{N}\sum_{n=1}^{N}[-u'v'I_{i,H}(u',v')]_n, \tag{4}$$

$$I_{i,H}(u',v') = \begin{cases} 1, & \text{if } (u',v') \text{ in quadrant } i \text{ and } |u'v'| < H(u'_{\mathrm{rms}}v'_{\mathrm{rms}}) \\ 0, & \text{otherwise} \end{cases}, \tag{5}$$

where $H$ is the hole filtering parameter, and $u'_{\mathrm{rms}}$, $v'_{\mathrm{rms}}$ denote the root mean square values of velocity fluctuations $u'$ and $v'$, respectively. Consequently, only when $|u'v'| > H(u'_{\mathrm{rms}}v'_{\mathrm{rms}})$, is its contribution to different quadrants considered. Hereafter, the hole filtering parameter $H$ is referred to as the "hole size." An increase in the hole size leads to a higher percentage of small-magnitude velocity fluctuations being filtered out, thereby an increase in the contribution of extreme events.

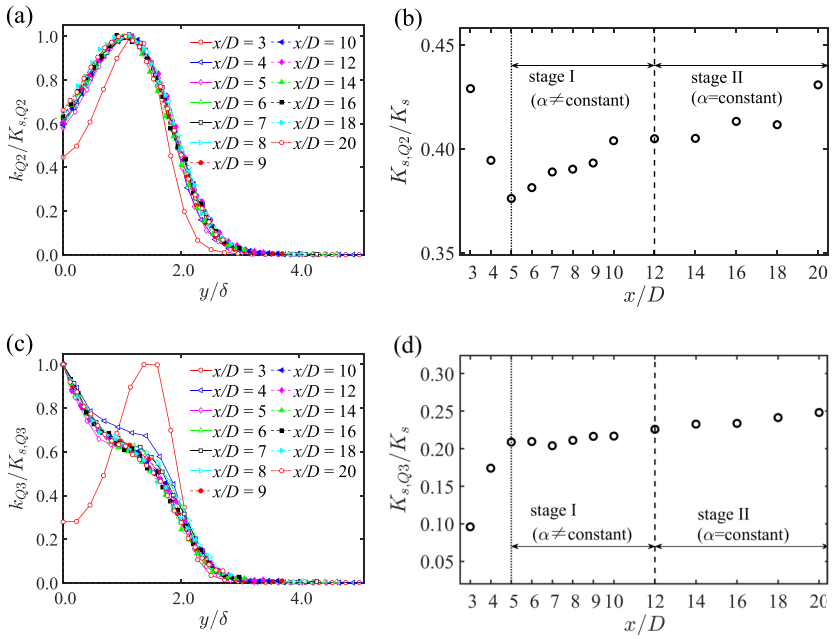


FIG. 9. Self-similarity and scaling law of $k_{Q2}$ and $k_{Q3}$. (a), (c) The normalized profiles of $k_{Q2}$ and $k_{Q3}$; (b), (d) the streamwise evolution of the ratio $K_{s,Q2}/K_s$ and $K_{s,Q3}/K_s$. The vertical dotted and dashed lines in (b) and (d), denoting the start position of self-similarity stage I ($\alpha \neq$ constant) and self-similarity stage II ($\alpha =$ constant), respectively, are plotted based on Ref. [9].

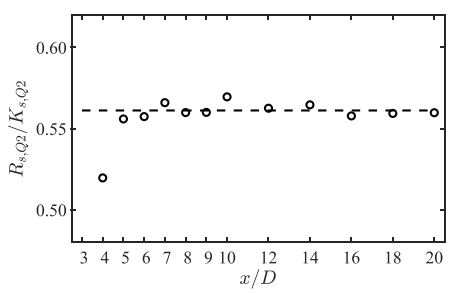


FIG. 10. Streamwise evolution of the ratio $R_{s,Q2}/K_{s,Q2}$.

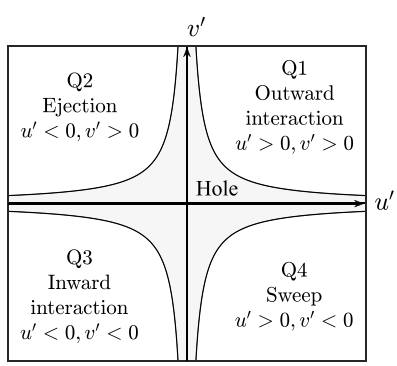


FIG. 11. Illustration of hole filtering method.

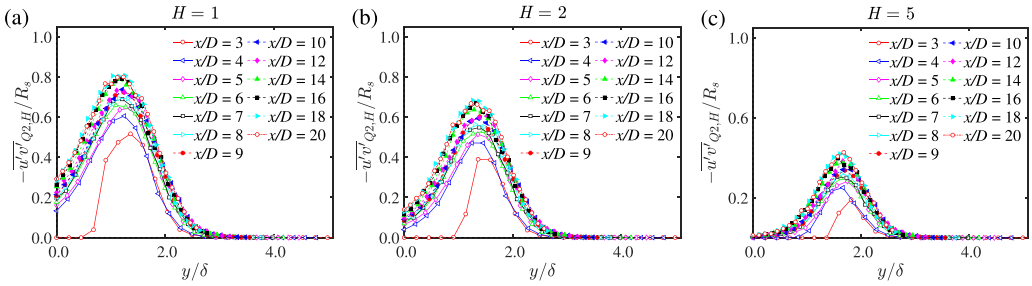


FIG. 12. Normalized lateral profiles of $-\overline{u'v'}_{Q2,H}$ by $R_s$ with hole size (a) $H = 1$, (b) $H = 2$, and (c) $H = 5$.

The normalized lateral profiles of $-\overline{u'v'}_{Q2,H}$ for various hole sizes $H$ are presented in Fig. 12. As expected, the value of $-\overline{u'v'}_{Q2,H}$ decreases as the hole size $H$ increases. Another finding is that the hole size $H$ has no effect on the length scaling of the lateral profiles of $-\overline{u'v'}_{Q2,H}$. Figure 13 shows the profiles of $-\overline{u'v'}_{Q2,H}$ normalized by $R_{s,Q2,H}$ (defined in a similar manner as $R_{s,Q2}$ but with consideration of the hole filtering effect). These profiles can also be well collapsed into a single line in the region $x/D \geqslant 4$. Figure 14(a) shows that the choice of hole filtering size also has some influence on the normalized profiles of $-\overline{u'v'}_{Q2,H}$. More specifically, as the hole size $H$ increases, the peak position of the profiles shifts outward. Additionally, the symmetry of the normalized profiles improves with the increase of the hole size $H$. Moreover, Fig. 14(b) illustrates that $R_{s,Q2,H}/R_{s,Q2,H=0}$ remains roughly constant in the $x/D \geqslant 4$ region. This observation implies that the hole filtering does not affect the velocity scaling of the lateral profiles of $-\overline{u'v'}_{Q2,H}$. Figure 15 shows the profiles of $-\overline{u'v'}_{Q2,H}/R_{s,Q2,H=0}$. It is worth noting that $-\overline{u'v'}_{Q2,H}/R_{s,Q2,H=0}$ remains approximately equal to each other in the outer part of the wake for various hole sizes, as illustrated in Fig. 15. This finding suggests that the hole filtering has a negligible effect on $-\overline{u'v'}_{Q2}$ in the outer part of the wake. It is widely known that extreme events are more prevalent in the wake edge region [31–36], which shall be discussed in Sec. V below. Thus one may argue that extreme events are closely related to ejection events and thus are crucial to the momentum transport.

In conclusion, the distribution of the intense Reynolds shear stress in ejection quadrant $\overline{u'v'}_{Q2,H}$ can remain in a self-similar state. Besides, the hole size $H$ has some influence on the shape of the normalized profiles of $-\overline{u'v'}_{Q2,H}$, but not its length scaling and velocity scaling.

### C. Spectrum filtering effect on the self-similar state of different quadrant contributions

Small-magnitude velocity fluctuations are filtered out via the hole filtering method. However, small-magnitude velocity fluctuations can result from both small-scale and large-scale coherent

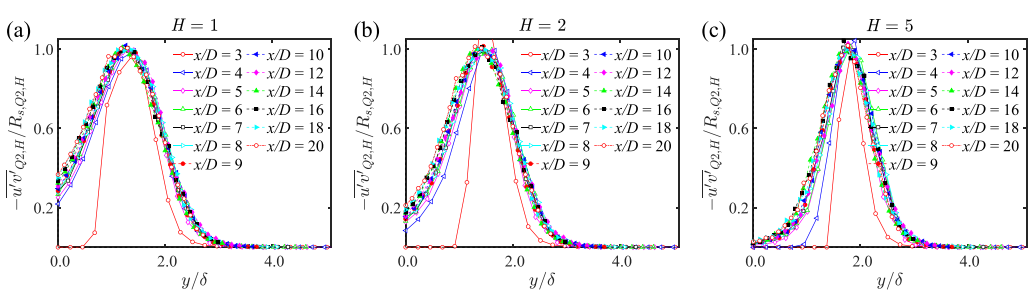


FIG. 13. Normalized lateral profiles of $-\overline{u'v'}_{Q2,H}$ by $R_{s,Q_2,H}$ with hole size (a) $H = 1$, (b) $H = 2$, and (c) $H = 5$.

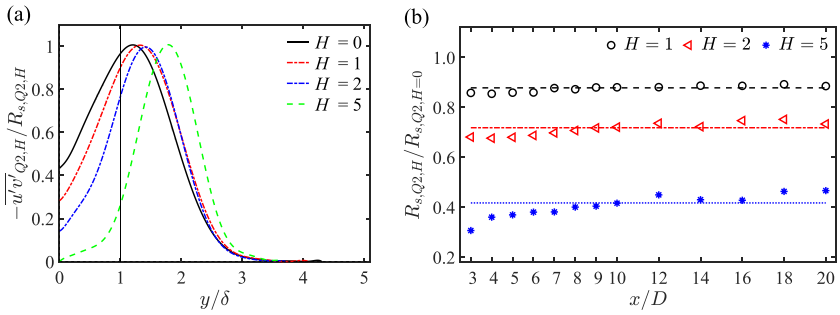


FIG. 14. (a) The fitted curve of the normalized lateral profiles of $-\overline{u'v'}_{Q2,H}$. (b) The streamwise evolution of the ratio $R_{s,Q2,H}/R_{s,Q2,H=0}$.

structures. To delve into the contribution of large-scale coherent structures, the spectrum filtering method is applied in this section.

Figure 16 shows an illustration of low-pass filtering of the spectrum of $u'$ and the cross-spectrum of $u'$ and $v'$ at $x/D = 14$, $y/D = 1.6$, where the velocity fluctuations above a certain frequency are filtered out. Based on Taylor's frozen hypothesis, low-pass filtering implies that the coherent structures below a specific length scale are filtered out. Note that spectrum filtering is computed via Python's zero-phase digital filtering function *filtfilt*.

Firstly, the effect of spectrum filtering on the self-similarity and scaling of the lateral profiles of $-\overline{u'v'}$ is analyzed. Figure 17 shows the normalized profiles of the spectrum-filtered Reynolds shear stress $-\overline{u'v'}_f$. It is clear that these normalized profiles can be well collapsed into a single line, although there is a slight discrepancy noted for the smallest filtering frequency $f_s D/U_\infty = 0.16$, which is likely to be mitigated by employing longer sampling times. Figure 18 shows the streamwise evolution of $R_{s,f_s}/R_s$. Here $R_{s,f_s}$ represents the square value of the characteristic velocity scale of the lateral profiles of $-\overline{u'v'}_f$ with filtering frequency $f_s$. As shown in Fig. 18, the ratio $R_{s,f_s}/R_s$ remains approximately constant within the measurement region of the present study. This finding suggests that the spectrum filtering does not impact the scaling of the characteristic velocity scale of the lateral profiles of $-\overline{u'v'}$, at least within a specified frequency range. Consequently, data sets obtained with relatively lower sampling frequency, i.e., data sets obtained using anemometers (with typical sampling frequencies of 1–30 Hz [48–52]), may be sufficient for the scaling analysis.

The effect of the cutoff frequency selection on the self-similarity of the ejection contribution to $-\overline{u'v'}_f$ ($-\overline{u'v'}_{Q2,f}$) is analyzed. Figure 19 shows the normalized profiles of $-\overline{u'v'}_{Q2,f}$. As shown in Figs. 19(a)–19(c), the choice of the cutoff frequency does impact the value of the characteristic velocity scale of the profiles of $-\overline{u'v'}_{Q2,f}$, while it does not affect the characteristic length scale. Figs. 19(d)–19(f) reveals that when normalized by $R_{s,Q2,f_s}$ and $\delta$, the normalized profiles can be

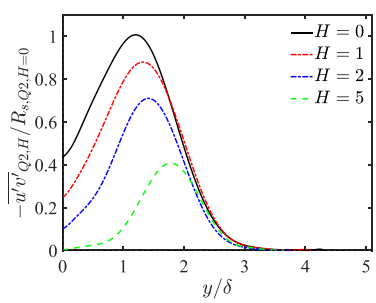


FIG. 15. The fitted curve of the lateral profiles of $-\overline{u'v'}_{Q2,H}$ normalized by $R_{s,Q2,H=0}$.

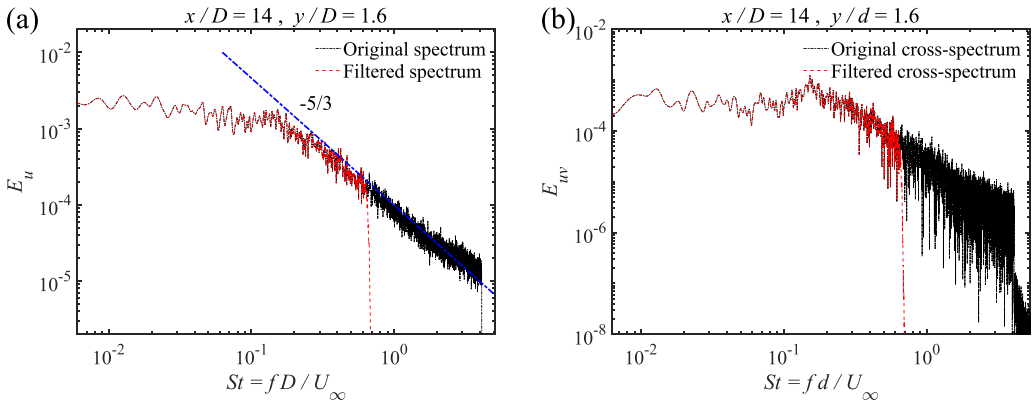


FIG. 16. Illustration of spectrum filtering on (a) the spectrum of $u'$, and (b) the cross-spectrum of $u'$ and $v'$. Note that the frequency scale that can be reached by the Cobra Probe used in the present study is 1250 Hz.

well collapsed into the same single line as the no spectrum-filtered case in the region $x/D \geqslant 4$, irrespective of the cutoff frequency. Note that the discrepancy is slightly large for the case of $f_s D/U_\infty = 0.16$. Moreover, Fig. 20 shows that $R_{s,Q2,f_s}/R_{s,Q2}$ remains approximately constant in the region $x/D \geqslant 4$, underscoring that the spectrum filtering does not affect the scaling law of the characteristic velocity scale of the lateral profiles of $-\overline{u'v'}_{Q2}$.

In conclusion, spectrum filtering exerts no influence on the shape of the normalized profiles of $-\overline{u'v'}$ and $-\overline{u'v'}_{Q2}$, nor their characteristic length scale. Moreover, while spectrum filtering does reduce the magnitude of $-\overline{u'v'}$ and $-\overline{u'v'}_{Q2}$, and consequently the corresponding characteristic velocity scale, it does not affect the scaling law of the characteristic velocity scale.

## V. QUADRANT CONTRIBUTION IN TIME SERIES AND ITS RELATION TO EXTREME EVENTS

The hole filtering analysis suggests a potential link between ejection events and extreme events, while spectrum filtering analysis reveals a connection between ejection events and large-scale coherent structures. In this section, the quadrant distribution in time series is analyzed to unveil the intricate relationship between extreme events and coherent structures and their relationship with different quadrant contributions.

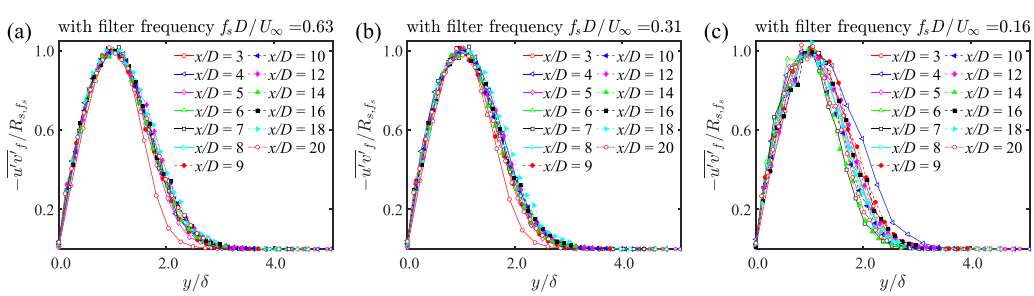


FIG. 17. The normalized lateral profiles of $-\overline{u'v'}_f$ with filter frequency (a) $f_s D/U_\infty = 0.63$, (b) $f_s D/U_\infty = 0.31$, and (c) $f_s D/U_\infty = 0.16$.

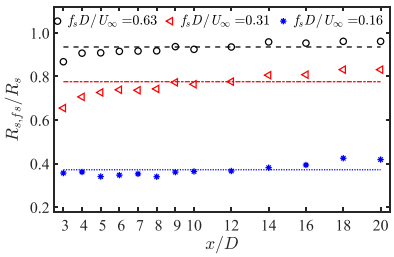


FIG. 18. Streamwise evolution of the ratio of the characteristic velocity scale of $-\overline{u'v'}_f$ with different filter frequencies.

Figure 21 shows the lateral profiles of skewness $S_u$ and kurtosis $K_u$ at $x/D = 20$, along with an illustrative example of the probability distribution function (PDF) of streamwise velocity fluctuation $u'$ at $x/D = 20$, $y/D = 1.6$, where $S_u$ and $K_u$ are defined as

$$S_u = \frac{\overline{u'^3}}{(\overline{u'^2})^{3/2}}, \tag{6}$$

$$K_u = \frac{\overline{u'^4}}{(\overline{u'^2})^2}. \tag{7}$$

As shown in Fig. 21, $S_u$ decreases in the lateral direction with $S_u < 0$ in the outer part of the wake, $K_u$ increases in the lateral direction with $K_u > 3$ in the outer part of the wake, and the PDF of $u'$ at $y/D = 1.6$ is characterized by a flatter left tail in contrast to the right tail. This indicates an increase in the occurrences of deceleration extreme events in the outer part of the wake [31–36].

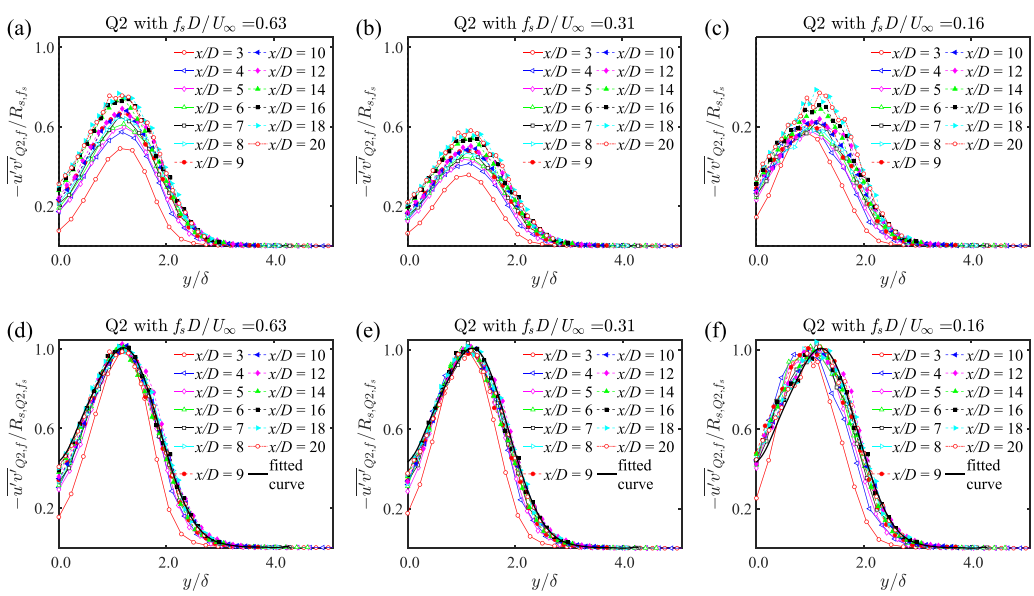


FIG. 19. Normalized lateral profiles of $-\overline{u'v'}_{Q2,f}$ by $R_{s,f_s}$ with filter frequency (a) $f_sD/U_\infty = 0.63$, (b) $f_sD/U_\infty = 0.31$, and (c) $f_sD/U_\infty = 0.16$; and normalized lateral profiles of $-\overline{u'v'}_{Q2,f}$ by $R_{s,Q2,f_s}$ with filter frequency (a) $f_sD/U_\infty = 0.63$, (b) $f_sD/U_\infty = 0.31$, and (c) $f_sD/U_\infty = 0.16$. The black curve in (d), (e), and (f) is the fitted curve of the normalized profiles of $-\overline{u'v'}_{Q2}$.

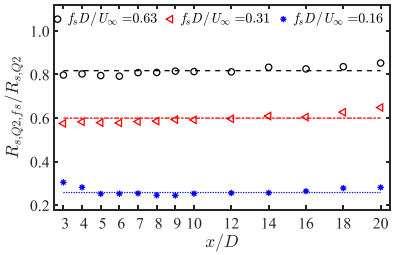


FIG. 20. Streamwise evolution of the ratio of the characteristic velocity scale of $-\overline{u'v'}_{Q2,f}$ with different filter frequencies.

Figure 22 shows the time evolution of streamwise velocity alongside its spectrum-filtered and hole-filtered versions within different quadrants at $x/D = 20,\ y/D = 1.6$. This visualization highlights how hole filtering eliminates small-magnitude fluctuations, retaining only large-magnitude fluctuations that are associated with extreme events. Figure 23(a) shows the PDF of hole-filtered $u'$. The pronounced hole-filtering effect is clear confined to the central region of the PDF, which further confirms these hole filtering effects. Note that Fig. 23(a) shows that the tail of the PDF of the hole-filtered $u'$ is slightly reduced compared to the original distribution. This is due to the fact that even during extreme events, some streamwise velocity fluctuations are filtered out due to the relatively small magnitude of lateral velocity fluctuation $v'$.

With respect to spectrum filtering, Fig. 22 illustrates that it smooths the time evolution of $u'$ through low-pass filtering, which results in a more pronounced reduction of the tail of the PDF of $u'$, as can be seen from Fig. 23(a). Moreover, Fig. 22 shows that after the low-pass spectrum filtering, both extreme events and other large-scale motions are still preserved, which can explain why the spectrum filter does not affect on the self-similarity of the normalized profiles of $-\overline{u'v'}_f$ and $-\overline{u'v'}_{Q2,f}$, as shown in Figs. 17 and 19. In addition, the positive part of the PDF of the spectrum-filtered $u'$ closely resembles a Gaussian function, indicating that the acceleration extreme events are filtered out. Thus, the size of the coherent structures related to the deceleration extreme events is much larger compared to those related to the acceleration extreme events.

Moreover, Fig. 22(b) also illustrates that the deceleration extreme events are mainly related to the ejection events. Figure 23(b) shows the PDF of different quadrants distribution of $u'$. As can be seen from Fig. 23(b), the left tail of the PDF of $u'$ is mainly due to the ejection contribution. This observation further emphasizes that the deceleration extreme events are primarily induced by ejection events. This correlation explains the observation that $-\overline{u'v'}_{Q2,H}/R_{s,Q2,H=0}$ remains approximately constant across various hole sizes, as shown in Fig. 15. Therefore, deceleration extreme events, large-scale coherent structures, and ejection events, serving as the dominant mechanisms in the outer part of the wake, are closely related to each other.

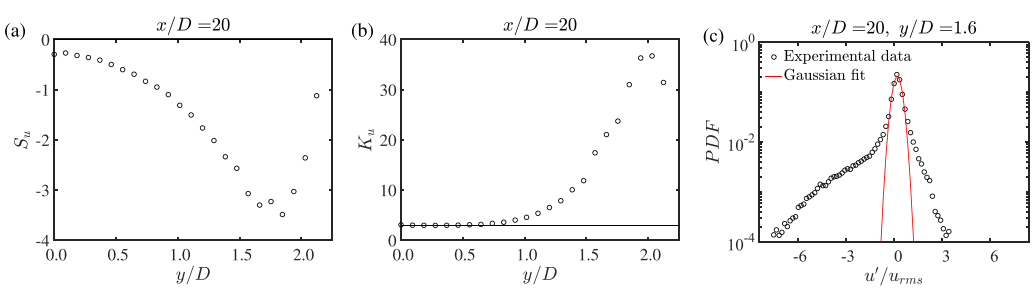


FIG. 21. Lateral profiles of (a) skewness, (b) kurtosis, and (c) probability distribution function of streamwise velocity fluctuation $u'$. The black horizontal line in subplot (b) represents $K_u = 3$.

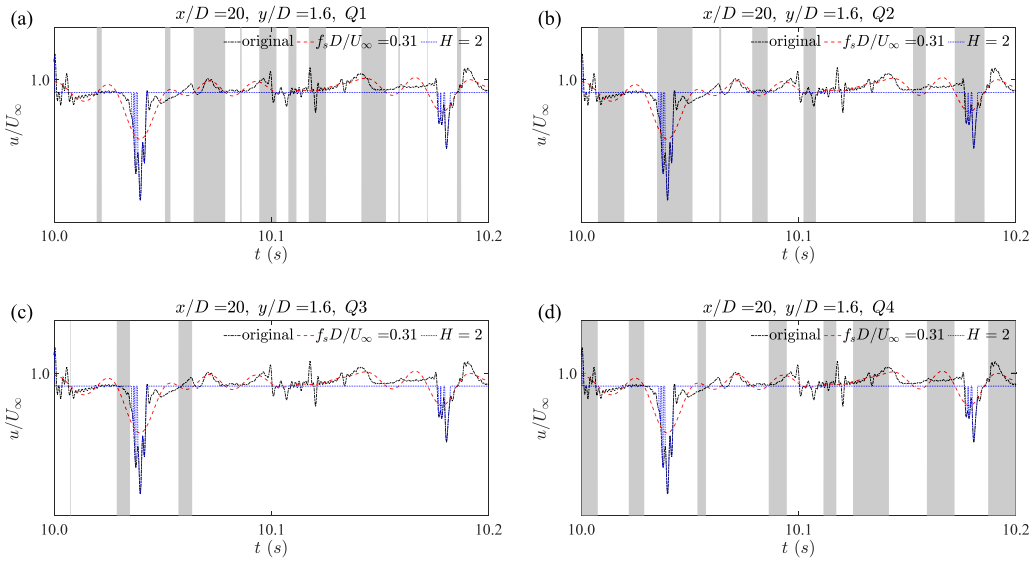


FIG. 22. Quadrant distribution in the time series of the streamwise velocity in quadrant (a) $Q1$, (b) $Q2$, (c) $Q3$, and (d) $Q4$. The shaded area represents the duration of the events in the corresponding quadrant.

In conclusion, deceleration extreme events, large-scale coherent structures, and ejection events, serving as the dominant mechanisms in the outer part of the wake, are closely related to each other. The size of the coherent structures related to the deceleration extreme events is much larger compared to those related to the acceleration extreme events.

## VI. CONCLUSION

A comprehensive quadrant analysis of the turbulent rotor wake is performed to investigate the self-similar state of single-point turbulent statistics across different quadrants. The effects of intense Reynolds shear stress and large-scale coherent structures on the self-similar state and scaling laws of the normalized profiles are analyzed. The main conclusions can be drawn as follows:

(1) The peak positions of the profiles of $-\overline{u'v'}_{Q2}$ and $-\overline{u'v'}_{Q4}$ are found to be approximately consistent with those of $k_{Q2}$ and $k_{Q4}$, respectively. Indicating a strong correlation between $-\overline{u'v'}_{Q2}$ and $k_{Q2}$, as well as a notable correlation between $-\overline{u'v'}_{Q4}$ and $k_{Q4}$. Sweeps and ejections detected

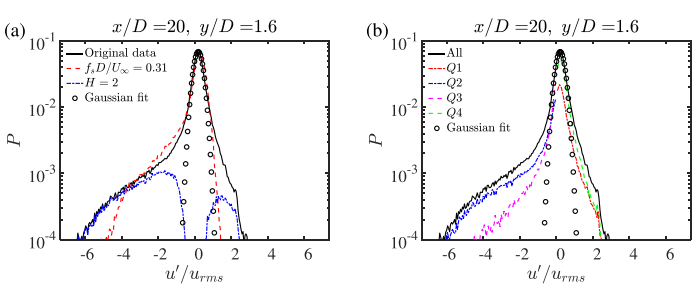


FIG. 23. (a) Filtering effects on the probability distribution function of the streamwise velocity fluctuations. (b) Contribution of different quadrants to the probability distribution function of the streamwise velocity fluctuation.

by quadrant analysis are closely related to coherent structures, thus, the high conventional turbulent kinetic energy at the wake center is mainly attributed to small-scale coherent structures.

(2) In the wake self-similar region, the lateral profiles of $-\overline{u'v'}_{Qi}$ and $k_{Qi}$ can also reach a self-similar state. The length scaling is the same for the profile of $-\overline{u'v'}$, $k$, and their different quadrant contributions. However, the velocity scaling of their distribution in $Q2$ and $Q3$ is different. Moreover, their distribution in $Q2$ and $Q3$ reaches a state of self-similarity stage II ($\alpha =$ constant) farther downstream compared to the streamwise evolution of the self-similarity stage of the wake.

(3) The exploration of the intense Reynolds shear stress reveals that the choice of hole filtering size has some influence on the shape of the normalized profiles of $-\overline{u'v'}_{Q2}$, but does not affect their self-similar state, length scaling and velocity scaling. Therefore, to some extent, provides some support for the self-similarity of the distribution of coherent structures in turbulent wake. Additionally, the hole filtering effect on $-\overline{u'v'}_{Q2}$ is negligible in the outer part of the wake, indicating a close interrelationship between ejection events and deceleration extreme events.

(4) The exploration of the contributions of different scale coherent structures reveals that the choice of cutoff frequency has no impact on the self-similarity of the lateral profiles of $-\overline{u'v'}$ and $-\overline{u'v'}_{Q2}$, including the shape of the normalized profiles and the length scale. For the characteristic velocity scale of $-\overline{u'v'}$ and $-\overline{u'v'}_{Q2}$, spectrum filtering reduces their magnitude without affecting their scaling.

(5) Quadrant analysis of the temporal evolution of velocity fluctuations reveals a close interrelationship among ejection events, large-scale coherent structures, and deceleration extreme events, which serve as the predominant mechanisms in the outer part of the wake. Moreover, the size of the coherent structures related to the deceleration extreme events is much larger compared to those related to the acceleration extreme events.

This study explores the self-similar state of different quadrant contributions and elucidates the intricate relationships among large-scale coherent structures, deceleration extreme events, and ejection events. The spatio-temporal evolution of coherent structures and energy transportation in turbulent wakes shall be studied in future work.

## ACKNOWLEDGMENTS

This study was cosupported by the National Natural Science Foundation of China (Grants No. 52306249, No. 91952105, No. 51921006, No. 51878230, and No. 52178470), the Six Talent Peaks Project in Jiangsu Province (Grant No. 2019-SZCY-005), the Department of Science and Technology of Guangdong Province (Grant No. 2020B1212030001), the Natural Science Foundation of Heilongjiang Province (Grant No. YQ2021E033), the Postdoctoral Scientific Research Development Fund of Heilongjiang Province (Grant No. LBH-Q20021), the Heilongjiang Touyan Team, and the Fundamental Research Funds for Central University (Grants No. 30918011325 and No. 921011212).

[1] H. Tennekes and J. L. Lumley, *A First Course in Turbulence* (MIT Press, Massachusetts, 1972).

[2] A. Townsend, *The Structure of Turbulent Shear Flow* (Cambridge University Press, Cambridge, 1976).

[3] W. K. George, The self-preservation of turbulent flows and its relation to initial conditions and coherent structures, Adv. Turbul. **3973**, 75 (1989).

[4] J. Nedić, J. C. Vassilicos, and B. Ganapathisubramani, Axisymmetric turbulent wakes with new nonequilibrium similarity scalings, Phys. Rev. Lett. **111**, 144503 (2013).

[5] T. Dairay, M. Obligado, and J. C. Vassilicos, Non-equilibrium scaling laws in axisymmetric turbulent wakes, J. Fluid Mech. **781**, 166 (2015).

[6] K. Chongsiripinyo and S. Sarkar, Decay of turbulent wakes behind a disk in homogeneous and stratified fluids, J. Fluid Mech. **885**, A31 (2020).
[7] J. Ortiz-Tarin, S. Nidhan, and S. Sarkar, High-Reynolds-number wake of a slender body, J. Fluid Mech. **918**, A30 (2021).
[8] D. C. Saunders, J. A. Britt, and S. Wunsch, Decay of the drag wake of a sphere at Reynolds number $10^5$, Exp. Fluids **63**, 71 (2022).
[9] X.-L. Xiong, S. Laima, and H. Li, Novel scaling laws in the nonequilibrium turbulent wake of a rotor and a fractal plate, Phys. Fluids **34**, 065130 (2022).
[10] G. I. Barenblatt, *Scaling*, Cambridge Texts in Applied Mathematics Vol. 34 (Cambridge University Press, Cambridge, 2003).
[11] M. Bastankhah and F. Porté-Agel, A new analytical model for wind-turbine wakes, Renewable Energy **70**, 116 (2014).
[12] R. J. Stevens and C. Meneveau, Flow structure and turbulence in wind farms, Annu. Rev. Fluid Mech. **49**, 311 (2017).
[13] C. Meneveau, Big wind power: seven questions for turbulence research, J. Turbul. **20**, 2 (2019).
[14] V. P. Stein and H.-J. Kaltenbach, Non-equilibrium scaling applied to the wake evolution of a model scale wind turbine, Energies **12**, 2763 (2019).
[15] X.-L. Xiong, P. Lyu, W.-L. Chen, and H. Li, Self-similarity in the wake of a semi-submersible offshore wind turbine considering the interaction with the wake of supporting platform, Renewable Energy **156**, 328 (2020).
[16] Z. Li and X. Yang, Large-eddy simulation on the similarity between wakes of wind turbines with different yaw angles, J. Fluid Mech. **921**, A11 (2021).
[17] X.-L. Xiong, S. Laima, and H. Li, Asymmetries and similarities of yawed rotor wakes, Phys. Fluids **34**, 105110 (2022).
[18] X.-L. Xiong, S. Laima, and H. Li, Experimental study of the wake of multi-rotor turbine, Ocean Eng. **269**, 113594 (2023).
[19] Y. Zhang, Z. Li, X. Liu, F. Sotiropoulos, and X. Yang, Turbulence in waked wind turbine wakes: Similarity and empirical formulae, Renewable Energy **209**, 27 (2023).
[20] J. Vassilicos, From Tennekes and Lumley to Townsend and to George: A slow march to freedom, in *Whither Turbulence and Big Data in the 21st Century?* edited by A. Pollard, L. Castillo, L. Danaila, and M. Glauser (Springer, 2016), pp. 3–11.
[21] J. Philip and I. Marusic, Large-scale eddies and their role in entrainment in turbulent jets and wakes, Phys. Fluids **24**, 055108 (2012).
[22] J. Chen, R. Antonia, and Y. Zhou, Relationship between coherent Reynolds shear stress and large-scale vortical structures, Phys. Fluids **35**, 021706 (2023).
[23] D. Küchemann, Report on the I.U.T.A.M. symposium on concentrated vortex motions in fluids, J. Fluid Mech. **21**, 1 (1965).
[24] J. M. Wallace, H. Eckelmann, and R. S. Brodkey, The wall region in turbulent shear flow, J. Fluid Mech. **54**, 39 (1972).
[25] L. Lignarolo, D. Ragni, F. Scarano, C. S. Ferreira, and G. Van Bussel, Tip-vortex instability and turbulent mixing in wind-turbine wakes, J. Fluid Mech. **781**, 467 (2015).
[26] K. Viestenz and R. B. Cal, Streamwise evolution of statistical events in a model wind-turbine array, Boundary Layer Meteorol. **158**, 209 (2016).
[27] W. Yin, S. Tao, K. Nagata, Y. Ito, Y. Sakai, and Y. Zhou, Spatial distribution of coherent structures in a self-similar axisymmetric turbulent wake, Phys. Rev. Fluids **8**, 084603 (2023).
[28] R. Antonia and L. Browne, Quadrant analysis in the turbulent far-wake of a cylinder, Fluid Dyn. Res. **2**, 3 (1987).
[29] J. M. Wallace, Quadrant analysis in turbulence research: History and evolution, Annu. Rev. Fluid Mech. **48**, 131 (2016).
[30] K. Nolan, E. Walsh, and D. McEligot, Quadrant analysis of a transitional boundary layer subject to free-stream turbulence, J. Fluid Mech. **658**, 310 (2010).

[31] Y. Zhou, K. Nagata, Y. Sakai, H. Suzuki, Y. Ito, O. Terashima, and T. Hayase, Development of turbulence behind the single square grid, Phys. Fluids **26**, 045102 (2014).
[32] S. Laizet, J. Nedić, and J. C. Vassilicos, The spatial origin of $-5/3$ spectra in grid-generated turbulence, Phys. Fluids **27**, 065115 (2015).
[33] I. Paul, G. Papadakis, and J. Vassilicos, Genesis and evolution of velocity gradients in near-field spatially developing turbulence, J. Fluid Mech. **815**, 295 (2017).
[34] Y. Zhou, K. Nagata, Y. Sakai, and T. Watanabe, Extreme events and non-Kolmogorov spectra in turbulent flows behind two side-by-side square cylinders, J. Fluid Mech. **874**, 677 (2019).
[35] Y. Zhou, K. Nagata, Y. Sakai, T. Watanabe, Y. Ito, and T. Hayase, Energy transfer in turbulent flows behind two side-by-side square cylinders, J. Fluid Mech. **903**, A4 (2020).
[36] H. Moffatt, Extreme events in turbulent flow, J. Fluid Mech. **914**, F1 (2021).
[37] S. Aubrun, S. Loyer, P. E. Hancock, and P. Hayden, Wind turbine wake properties: Comparison between a non-rotating simplified wind turbine model and a rotating model, J. Wind Eng. Ind. Aerodyn. **120**, 1 (2013).
[38] E. H. Camp and R. B. Cal, Mean kinetic energy transport and event classification in a model wind turbine array versus an array of porous disks: Energy budget and octant analysis, Phys. Rev. Fluids **1**, 044404 (2016).
[39] L. Lignarolo, D. Ragni, C. Ferreira, and G. Van Bussel, Experimental comparison of a wind-turbine and of an actuator-disc near wake, J. Renewable Sustainable Energy **8**, 023301 (2016).
[40] L. E. Lignarolo, D. Mehta, R. J. Stevens, A. E. Yilmaz, G. van Kuik, S. J. Andersen, C. Meneveau, C. J. Ferreira, D. Ragni, J. Meyers *et al.*, Validation of four LES and a vortex model against stereo-PIV measurements in the near wake of an actuator disc and a wind turbine, Renewable Energy **94**, 510 (2016).
[41] I. Neunaber, M. Hölling, J. Whale, and J. Peinke, Comparison of the turbulence in the wakes of an actuator disc and a model wind turbine by higher order statistics: A wind tunnel study, Renewable Energy **179**, 1650 (2021).
[42] M. K. Vinnes, S. Gambuzza, B. Ganapathisubramani, and R. J. Hearst, The far wake of porous disks and a model wind turbine: Similarities and differences assessed by hot-wire anemometry, J. Renewable Sustainable Energy **14**, 023304 (2022).
[43] L. P. Chamorro, R. E. Arndt, and F. Sotiropoulos, Reynolds number dependence of turbulence statistics in the wake of wind turbines, Wind Energy **15**, 733 (2012).
[44] J.-P. Hickey, F. Hussain, and X. Wu, Role of coherent structures in multiple self-similar states of turbulent planar wakes, J. Fluid Mech. **731**, 312 (2013).
[45] H. Schlichting and J. Kestin, *Boundary Layer Theory* (Springer, New York, 1961), Vol. 121.
[46] G. Cafiero, M. Obligado, and J. C. Vassilicos, Length scales in turbulent free shear flows, J. Turbul. **21**, 243 (2020).
[47] J. C. Vassilicos, Dissipation in turbulent flows, Annu. Rev. Fluid Mech. **47**, 95 (2015).
[48] J. Wyngaard, Cup, propeller, vane, and sonic anemometers in turbulence research, Annu. Rev. Fluid Mech. **13**, 399 (1981).
[49] H. Ren, S. Laima, W.-L. Chen, B. Zhang, A. Guo, and H. Li, Numerical simulation and prediction of spatial wind field under complex terrain, J. Wind Eng. Ind. Aerodyn. **180**, 49 (2018).
[50] I. Suomi and T. Vihma, Wind gust measurement techniques—From traditional anemometry to new possibilities, Sensors **18**, 1300 (2018).
[51] S. Li, E. Kaiser, S. Laima, H. Li, S. L. Brunton, and J. N. Kutz, Discovering time-varying aerodynamics of a prototype bridge by sparse identification of nonlinear dynamical systems, Phys. Rev. E **100**, 022220 (2019).
[52] S. Li, S. Laima, and H. Li, Physics-guided deep learning framework for predictive modeling of bridge vortex-induced vibrations from field monitoring, Phys. Fluids **33**, 037113 (2021).